

The Thermal Environment of the Fiber Glass Dome for the New Solar Telescope at Big Bear Solar Observatory

A. P. Verdoni^a, C. Denker^{a,b}, J. R. Varsik^c, S. Shumko^c, J. Nenow^c, and R. Coulter^c

^aNew Jersey Institute of Technology, 323 Martin Luther King Blvd, Newark, NJ 07102, U.S.A.

^bAstrophysikalisches Institut Potsdam, An der Sternwarte 16, D-14482 Potsdam, Germany

^cBig Bear Solar Observatory, 40386 North Shore Lane, Big Bear City, CA 92314, U.S.A.

ABSTRACT

The New Solar Telescope (NST) is a 1.6-meter off-axis Gregory-type telescope with an equatorial mount and an open optical support structure. To mitigate the temperature fluctuations along the exposed optical path, the effects of local/dome-related seeing have to be minimized. To accomplish this, NST will be housed in a 5/8-sphere fiberglass dome that is outfitted with 14 active vents evenly spaced around its perimeter. The 14 vents house louvers that open and close independently of one another to regulate and direct the passage of air through the dome. In January 2006, 16 thermal probes were installed throughout the dome and the temperature distribution was measured. The measurements confirmed the existence of a strong thermal gradient on the order of 5° Celsius inside the dome. In December 2006, a second set of temperature measurements were made using different louver configurations. In this study, we present the results of these measurements along with their integration into the thermal control system (ThCS) and the overall telescope control system (TCS).

Keywords: solar telescopes — telescope control systems — thermal control — seeing

1. INTRODUCTION

Solar telescopes with an aperture larger than 1 meter face a variety of challenges, if they want to achieve diffraction-limited resolution. Site selection is of primary concern. In the context of the proposed 4-meter aperture Advanced Technology Solar Telescope (ATST), significant efforts were undertaken to identify the best site(s) for solar observations.^{1,2,3} Big Bear Solar Observatory (BBSO) was identified as one of three sites suitable for high-resolution solar observations. However, the seeing characteristics at BBSO – a mountain-lake site – are quite different³ from the two other mountain-island sites Haleakalā, Maui, Hawai'i (which was selected as the future ATST site) and Observatorio Roque de los Muchachos on La Palma, Spain. The lake effectively suppresses the ground-layer seeing and very good seeing conditions are encountered from sunrise to sunset. This makes BBSO ideally suited for solar activity monitoring and space weather studies⁴ combining synoptic with high-resolution capabilities. These site characteristics and scientific objectives are exactly what has motivated the design, development and now construction of NST.^{5,6}

Since instrument seeing is a severe issue for solar telescopes, most high-resolution solar telescopes were placed inside vacuum tanks. This approach, however, is no longer feasible for apertures larger than 1 meter, since the entrance window (or lens) would become too thick in order to withstand the vacuum. Therefore, the next generation of solar telescopes has to rely on “open-designs”, i.e., the optical support structure and optics will be exposed to the elements. This in turn requires a good understanding and control of the thermal environment in which the telescope is placed. In a first set of papers,^{7,8} we have described on how to integrate seeing measurements into the NST operations and introduced plans on how to implement the NST ThCS. In this study, we will discuss more details on the ThCS implementation, the design of the fiberglass dome (a smaller version of the SOuthern Astrophysical Research (SOAR) telescope dome,⁹ a detailed weather record for BBSO, temperature measurements inside the dome under varying observing conditions, and some implications for the thermal control of the primary mirror, which is a 1/5-scale model for the 8.4-meter off-axis segments of the Giant Magellan Telescope's primary mirrors.¹⁰



Figure 1. *Left.* Image of the new NST dome at BBSO. The smaller dome in the foreground houses the Earthshine and $H\alpha$ full-disk telescopes. In this image the shutter is closed and the iris is covering the dome's 2-meter circular aperture. *Right.* Inside view of the closed iris and the iris drive motors. The folded windscreen is visible at the bottom of the iris.

2. 5/8-SPHERE FIBERGLASS DOME AND LOUVER EXPERIMENTS

The new NST dome at BBSO is a 10-meter diameter 5/8 sphere with an over the top nesting shutter housing a 2-meter circular aperture. The dome was manufactured by MFG Ratech and is modeled after the dome for the SOAR telescope in Cerro Pachon, Chile.⁹ The SOAR dome is approximately twice the size of the NST with a diameter of 20 m. It has a similar over the top shutter with windscreen attachment. However, it does not have the 14 active damped louver assemblies, which are evenly spaced around NST's equator. The exterior of the NST dome is comprised of Fiberglass Reinforced Plastic (FRP) panels that are assembled in three ring sections, which are vertically split into two hemispheres by the dome slit. The sections are supported by two 10-meter diameter steel arch girders that serve as guides for the dome shutter. Both the panels and arches sit on top of a 9.2-meter diameter steel ring beam, which rotates on a 16 fixed-point bogie system allowing the dome, shutter and windscreen to track the telescope for maximum protection against the prevailing winds.

The left panel of Figure 1 shows the newly installed NST dome with the aperture pointing to the east. In this image the dome shutter is closed and the iris covers the 2-meter circular aperture. Housed in the smaller dome in the foreground are the BBSO Earthshine and $H\alpha$ full-disk telescopes. The right panel of Figure 1 depicts an inside view of the closed iris. At the bottom of the aperture panel is the collapsed, foldable wind screen. As the aperture panel raises and lowers, the wind screen unfolds covering the exposed portion of the dome slit. To test the structural integrity of the dome a stress analysis was performed. The analysis was based on the maximum operating snow and ice loading conditions. The conditions call for the dome to retain its structure with a snow depth of 1 m, an average dead load of 97 kg ft^2 with a peak dead load of 195 kg ft^2 , and an ice thickness of 0.05 m. A worst case stress analysis was performed with a peak dead load of 195 kg ft^2 and a 200 kph wind acting simultaneously. The result was that the 10 m diameter was in substantial conformance with the manufacturers requirements.

NST's 14 vent gates allow wind flushing of the dome interior. The gates are made of a heavy gauge extruded aluminum, which is rated to withstand a wind load of approximately 190 kg m^{-2} . Each of the vents is $0.6 \text{ m} \times 1.8 \text{ m}$ with a depth of approximately 0.1 m. A damper is attached to each vent, which allows control over the amount and direction of air flow through the dome. The dampers will be activated based on the direction of the wind, measured by a weather station outside the dome, and the temperature gradients inside the dome, measured by 16 temperature probe units arranged symmetrically throughout the dome interior.⁶

The left panel of Figure 2 is an image of the inside of the dome showing three vent gate assemblies. The two motors responsible for opening and closing the vent louver system. To eliminate the presence of a thermal gradient inside the dome, the dome volume must be flushed 20 or more times per hour, which requires a wind speed of approximately $2 \text{ to } 3 \text{ m s}^{-1}$. BBSO benefits from a predominately westerly winds with a mean speed of

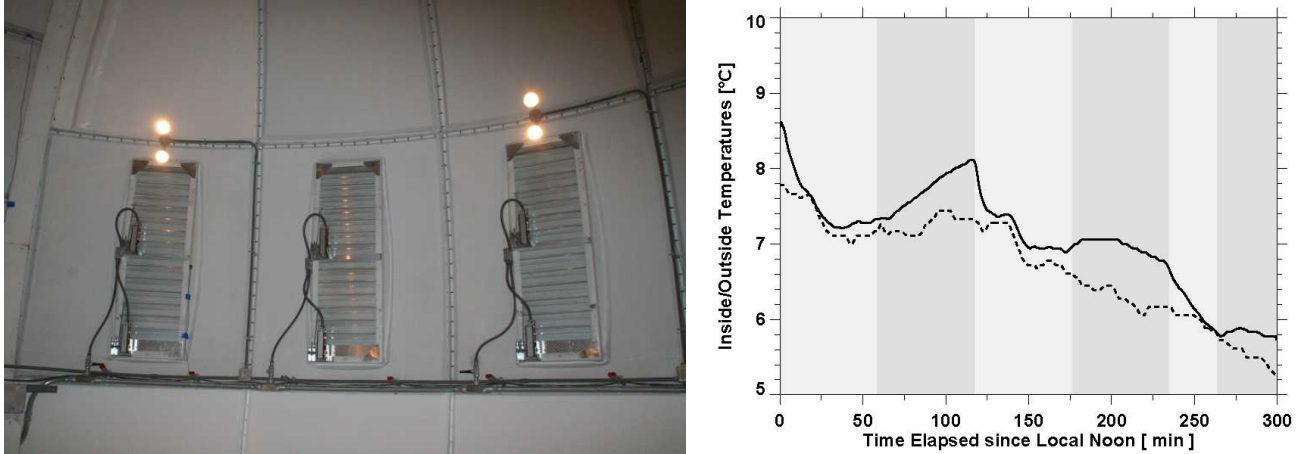


Figure 2. *Left.* The inside of the dome showing three of the active vent gate assemblies. Visible on each of the vents are the two motors that adjust the damper settings. *Right.* Temperature measured by one thermal probe (solid line) inside of the dome and the outside temperature (dashed line) as recorded by the weather station. The alternating light and dark stripes correspond to the open and closed configurations of the 14 louvers, respectively.

6 m s^{-1} .³ With a total dome volume of 330 m^3 , this is sufficient to achieve a flushing rate of 30 dome volumes per hour.

In January 2006, the first set of 16 temperature sensors were installed on the interior surface of the NST dome. The dome structure, skin, and louvers were installed at this time. However, the dome drive and shutter motors were not yet operational. The temporal evolution of the dome temperature was measured throughout the course of the day showing the existence of thermal gradients on the order of 10° C or more. In December 2006, with control of the dome drive and shutter motors being available, we were able to monitor the temporal evolution of the dome temperature while simultaneously opening and closing the louvers.

The dome shutter was closed as well as was the iris. The aperture was pointing to the west and remained in this position for the duration of the experiment. To control the opening and closing of the louvers the positions were set manually. The probe temperatures were obtained once every minute by polling the Temp-Trax Model E16 tracking thermometer using a Perl script running on a BBSO server. The configurations for the louvers were decided upon a priori and then executed. Along with the thermal probe data the corresponding weather station data was downloaded from the weather station.

The right panel of Figure 2 shows the results of a louver experiment conducted on December 12, 2006. The y -axis is temperature in degrees Celsius and the x -axis displays the minutes elapsed since local noon. The dark and light stripes of the background correspond to all 14 louvers being open or closed, respectively. The solid line is the temperature measured by a single thermal probe and the dashed line is the outside temperature measured by the weather station. The louvers are opened and closed every hour for the first four hours, then opened for a half hour and closed ending the run. The objective will be to determine with a good degree of accuracy the response time of the internal dome temperature with respect to louver configuration. Looking at the plot one can immediately see that the temperature inside of the dome follows the general trend of the exterior temperature. The opening and closing of the louvers is also apparent. When the louvers are open the temperature shows a characteristic decline until the interior and exterior are in close agreement. When the louvers are closed the temperature inside the dome climbs to approximately 1° C above the outside temperature. For more accurate results these experiments should be carried out with the NST present to ensure that all thermal sources are accounted for.

3. METEOROLOGICAL DATA

An accurate characterization of the meteorological conditions in the immediate surroundings of an observatory is important for daily and seasonal operations of the telescope. In February 2005, a Vantage Pro2 Plus weather

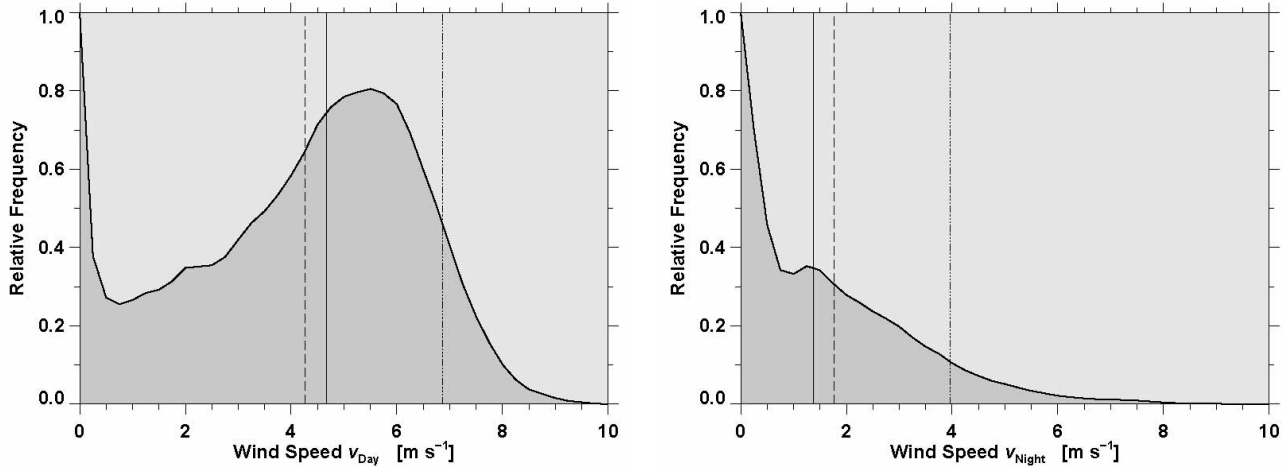


Figure 3. Frequency distributions of the wind speeds v_{Day} (left) and v_{Night} (right). The median, mean, and 10th percentile wind speeds are indicated by solid, dashed, and dashed-dotted vertical lines, respectively.

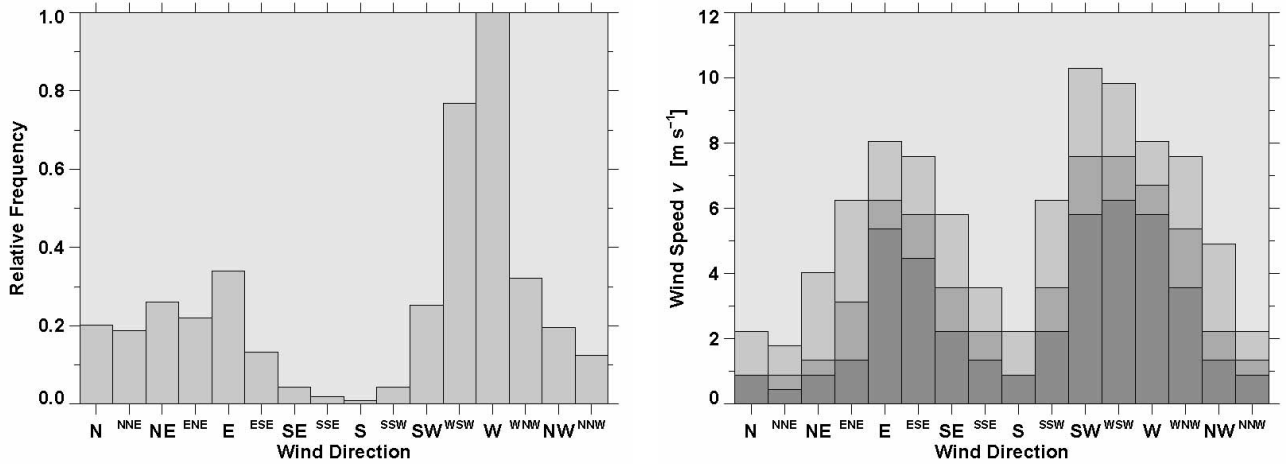


Figure 4. Left. Frequency distribution of the wind directions. Right. The median wind speed as a function of the wind direction is shown as dark gray. The lighter grays correspond to the 10th and 30th percentile of the respective frequency distributions.

station manufactured by Davis Instruments (<http://www.davisnet.com/>) was installed at BBSO to monitor these conditions. The weather station is outfitted with an integrated suite of meteorological instruments including solar radiation and UV sensors. Temperature and humidity sensors are housed inside a radiation shield for improved accuracy. The weather station data presented in this section covers 741 days from February 28, 2005 to March 10, 2007. The data was sampled at a 1-minute cadence with the exception of the first 10 days, when a cadence was 5 min.

The frequency distributions of daytime (left) and nighttime (right) wind speeds are shown in Figure 3. The median wind speed during the daytime is 4.67 m s^{-1} with a mean of 4.27 m s^{-1} . The 10th percentile (6.87 m s^{-1}) of the wind speed distribution was computed to provide an estimate for high wind conditions. During the night, the winds decrease in strength. The median, mean, and 10th percentile wind speeds are 1.38 m s^{-1} , 1.76 m s^{-1} , and 3.97 m s^{-1} , respectively. The median, mean and 10th percentile values for each of the distributions are represented by a solid, dashed, and dashed-dotted vertical line in Figure 3. The two wind speed distributions clearly show different characteristics. Much higher velocities are encountered during the daytime with a well-defined maximum between 5.0 and 6.0 m s^{-1} . This maximum is basically absent in the nighttime distribution,

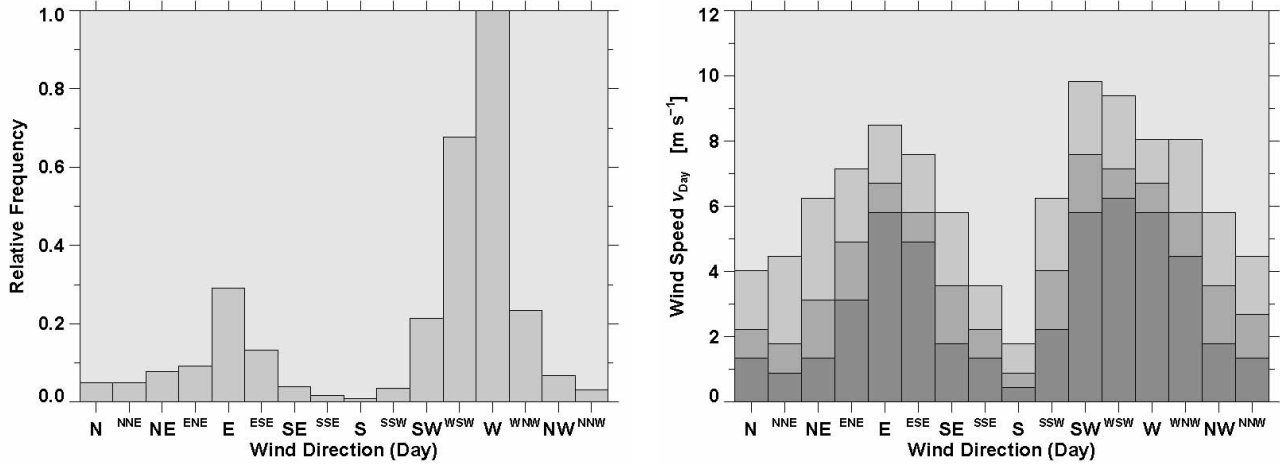


Figure 5. Frequency distribution of the daytime wind directions (same format as Figure 4).

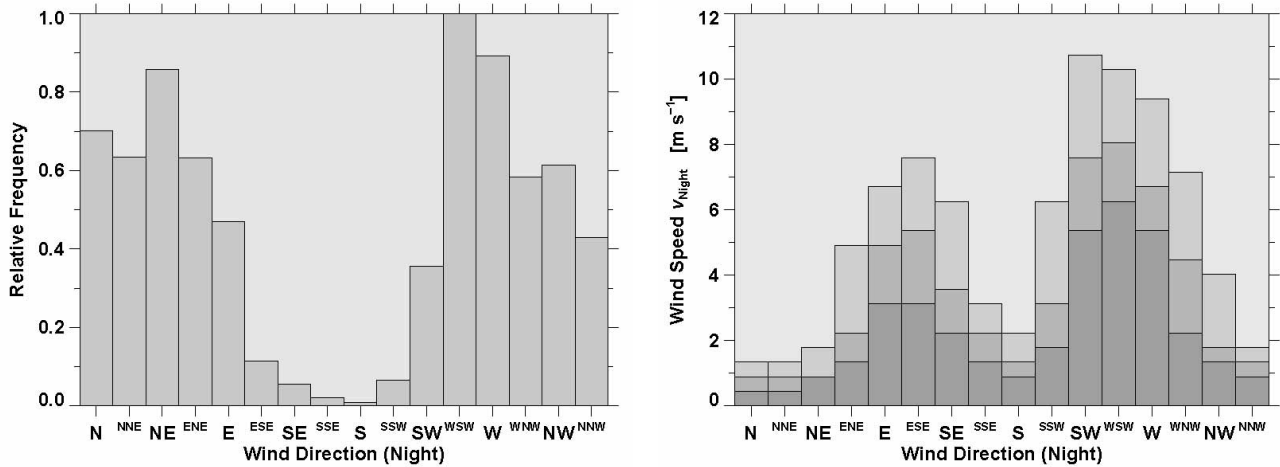


Figure 6. Frequency distribution of the nighttime wind directions (same format as Figure 4).

where we find a basically monotonic decrease of the frequency of occurrence with wind speed. The physical mechanism behind these discrepancies becomes more apparent in the frequency distribution of the directions (Figures 4).

The east-west orientation of Big Bear Lake and its mountain location gives rise to a unique distribution of wind directions. The relative frequency distribution of the wind direction is shown in the left panel of Figure 6 for the entire data set. The wind directions in the following plots are given on a the compass rose graduated into 16 sector. Immediately apparent is the predominance of westerly wind directions. This westerly wind is a result of gradient in pressure between the Los Angeles basing and the interior regions of the Southern Californian deserts.³ The winds are channeled through the canyons and valleys of the San Bernardino mountains. Since the wind does not encounter any obstruction passing over the cold waters of Big Bear Lake, the observatory island is embedded in almost laminar air flows. The water also provides a “heat sink” effectively suppressing ground-layer seeing. This is the explanation for the very good seeing conditions from sunrise to sunset at BBSO. A more quantitative picture of the wind speeds as a function of wind direction is presented in the right panel of Figure 4. Here, the gray scale corresponds (from dark to light) to the median, 10th and 30th percentile of the frequency distributions, respectively. For a westerly wind a median wind speed of approximately 6.0 m s^{-1} is measured with winds of 8 m s^{-1} or greater occurring 30 percent of the time. For easterly wind directions,

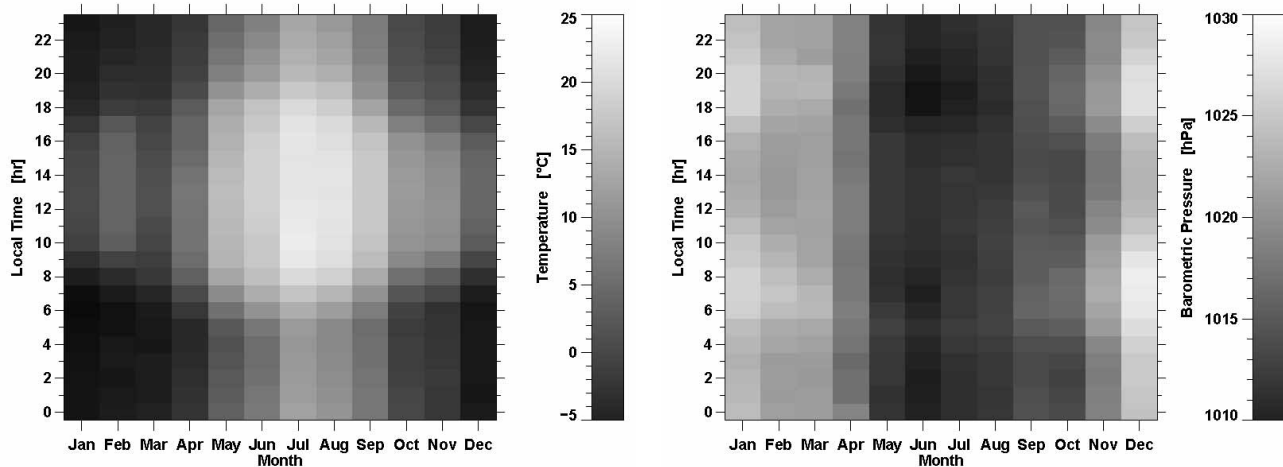


Figure 7. *Left.* Seasonal and diurnal variation of median temperature. *Right.* Seasonal and diurnal variation of median barometric pressure.

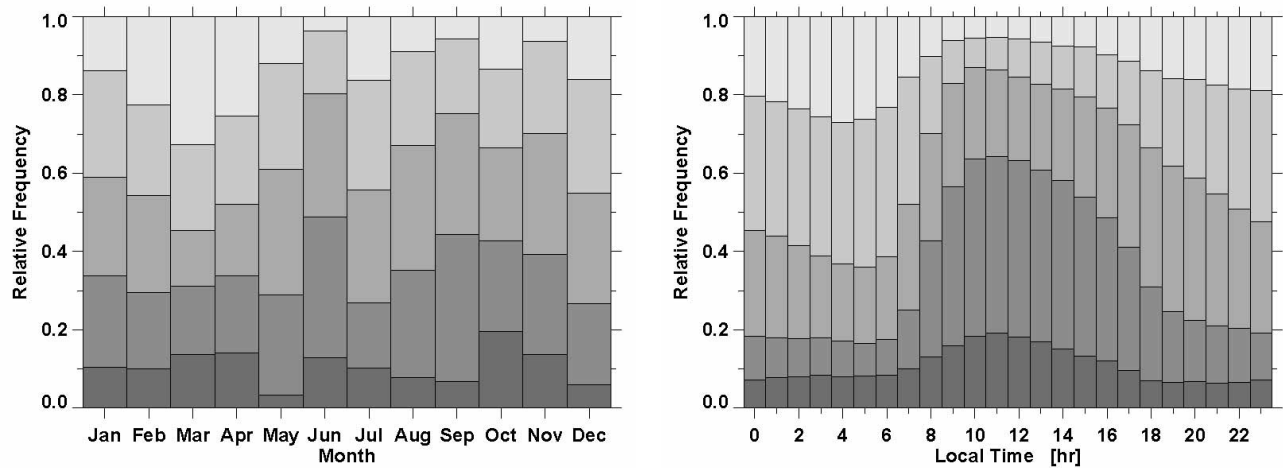


Figure 8. *Left.* Seasonal frequency distributions of the humidity. *Right.* Diurnal frequency distributions of the humidity. The gray scale (from dark to bright) corresponds to humidity levels of 20%, 40%, 60%, and 80%.

the speeds are comparable to westerly winds. These winds are caused by a reversal of the pressure gradient and are commonly referred to as Santa Ana winds.¹¹ A detailed discussion of the daytime seeing characteristics at BBSO was presented in an earlier study³ based on data from the ATST site survey. However, due to the nature of the daytime seeing monitor no nighttime weather data was available. Since nighttime observations might be scheduled for NST and BBSO has an existing program for Earthshine observations,¹² we present in this study also the respective nighttime weather data. These data also further illustrate the two different observing regimes for day and night (Figures 5 and 6).

Separating the daytime and nighttime frequency distributions shows an even more pronounced east-west orientation of the winds during the day. It also shows that Santa Ana conditions do not very frequently occur (about 10% of the time). However, even under these conditions the seeing can be very good³ but the observing conditions suffer from a low sky transparency due to dust carried in from the deserts. The wind speeds are very similar (about 6.0 m s^{-1}) for winds from the East and West (see right panel in Figure 5. However, in the the North-South direction the wind speeds are reduced to about 1.5 m s^{-1} . Figure 6 for reveals the nighttime wind regime, which is dominated by mountain down-slope winds. The air that has been heated during the day, now slowly flows down the mountain slope towards the cool surface of the lake. With the exception of the southern

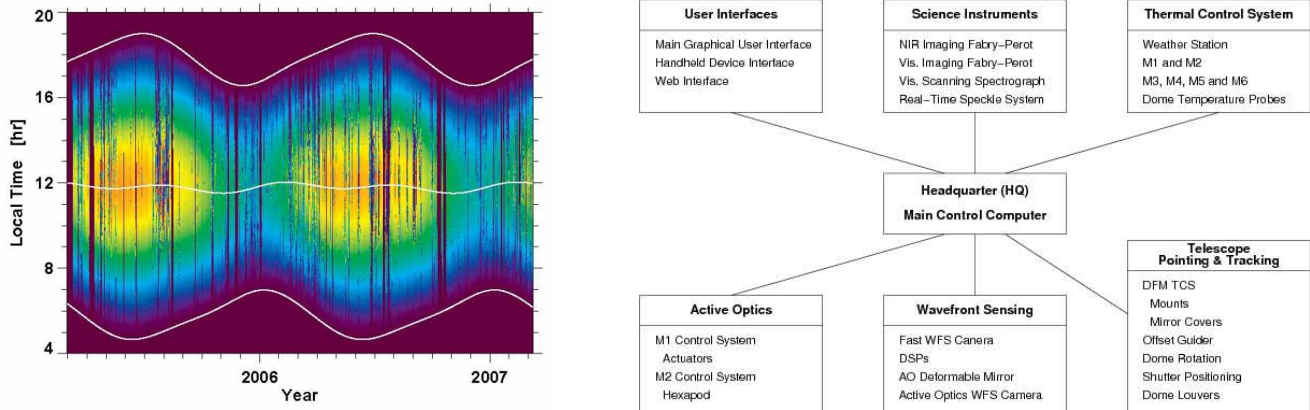


Figure 9. *Left.* Diurnal and seasonal variation of the solar radiation spanning the entire data set. The white contour lines refer to sunrise, local noon, and sunset. *Right.* Schematic overview of the main TCS components. The system components of the ThCS and TPTS, which are responsible for controlling the NST thermal environment, are shown on the right.

mountain slopes, there is no preferential direction for the down-slope winds but the wind speed distribution again follows the east-west orientation of Big Bear Valley. Consulting the wind speed distributions in Figure 3, low wind speed times $v < 1.0 \text{ m s}^{-1}$ occur during a significant fraction of time. This happens typically around dusk and dawn, when the change between the daytime and nighttime wind regime takes place.

In Figure 7, the seasonal and diurnal variations of the median temperature (*left*) and median barometric pressure (*right*) are shown as gray scales. The hottest month is July, when median temperatures reach about 25° C . The temperature spread between day and night is also much large during the summer months (about 10° C compared to 7° C in the winter). The warm temperatures in February might be an anomaly, since our data sample only covers slightly more than two years. The barometric pressure shown in the right panel of Figure 7 is basically inversely proportional to the temperature. The lowest values of the barometric pressure are measured throughout the summer months. The diurnal variations are more or less negligible. However, a small trend to higher barometric pressure can be observed around dusk and dawn, when transitioning from the daytime to the nighttime wind regime and vice versa. The seasonal trend of the barometric pressure is given by the pressure gradient between the coastal regions of Southern California and the inland deserts.

The seasonal (*left*) and diurnal (*right*) distributions of the humidity are shown in Figure 8. The gray scale corresponds (from dark to bright) to humidity levels of 20%, 40%, 60%, and 80%, respectively. The winter months and early spring is the most humid time of the year. Surprisingly, only a weak indication is found (in July) is visible for the monsoon season in July and August. Again, the explanation for this behavior is in the diurnal changes of the humidity. Shortly after sunrise, the air dries out and becomes least humid around local noon. With decreasing solar input in the afternoon, the humidity increases monotonically. This trend continues after sunset. The most humid time is reached just before sunrise. The high humidity during the night and dawn might cause problems for nighttime and Earthshine observations.

The weather station also included a solar radiometer. The left panel of Figure 9 displays the diurnal and seasonal variations of the solar radiation from which the clear time fraction (CTF) was computed. The solar radiation is displayed on a rainbow color scale, where violet corresponds to low light levels and orange/red refers the maximum of the solar radiation at noon in the summer time. Solar ephemeris computations including optical air mass were obtained from the Jet Propulsion Laboratory (JPL) Horizons web page (<http://ssd.jpl.nasa.gov/horizons.cgi>) to aid in the analysis.¹³ The ephemeris data were converted from Universal Time (UT) to Pacific Standard Time (PST, without daylight savings time correction) to match the weather station data. The three white lines (from bottom to top) refer to sunrise, local noon, and sunset, respectively. Especially in the winter and spring, entire days with low light levels are recorded. These times are during winter storms and when the sky is overcast. The monsoon season is also visible in the left panel of Figure 9 during the months of July and

August, when the daily radiation traces become spotty about two hours before local noon. During the monsoon the moist air and solar heating can give rise to severe thunderstorms. A threshold of 90% of the instantaneous solar radiation is used to compute the CTF. Since this fractional criterion becomes impractical for elevations lower than 5°, we only computed the CTF for higher elevation angles and extrapolated this value to the entire data set. The CTF determined from the solar radiation sensor of the weather station is 72.4%. This value agrees well with CTF value from the ATST site survey (71.2%)¹ and previous measurements obtained as part of the GONG site survey (70.7%).¹⁴

4. THERMAL CONTROL SYSTEM

The Thermal Control System (ThCS)⁸ is part of a distributed computer system, which controls the telescope, dome, adaptive optics (AO), and the post-focus instrumentation. The overall system is known as the Telescope Control System (TCS).¹⁵ A schematic overview of the TCS is shown in the right panel of Figure 9. Use of a distributed system allows for greater flexibility, and ultimately for greater simplicity than a monolithic design would provide. As a consequence, each subsystem within the TCS has only a limited set of tasks to perform.

Overall management of the TCS is carried out by the HQ (Headquarters) program running on a dedicated main control computer. HQ collects data from each subsystem for centralized logging and access by the main user GUI systems. Commands are sent from the GUIs to HQ for dispatch to the appropriate TCS system for execution. Each subsystem has an engineering GUI written in Java. In general, C++ and Java are the only languages used in the control system. The object-oriented TCS design has so far resulted in a successful implementation of all subsystems and significantly shortened the design and development time.¹⁶ Even though status information is provided by HQ to science instruments, they are currently not considered part of TCS. Instrument designers have to rely on well-defined interfaces implemented in the eXtended Markup Language (XML) to integrate the post-focus instruments in the hierarchical TCS infrastructure.

Communication within TCS is performed by Ethernet, which offers much better performance compared to older RS-232-based implementations and simplifies cabling to the telescope. Internet Communication Engine (ICE) from ZeroC was chosen as the standard communication protocol/software library. User interaction with all subsystems is handled by a system-wide main GUI, which accesses the subsystems through HQ. The HQ computer is also performing logging and archiving of status information, which is collected in a data base.

All high-level commands are written in XML. Commands, information requests, notifications, or error messages can be sent asynchronously. Fast network connectivity and generally short messages make the overhead of ASCII formatting negligible and does not result in any significant impact on overall performance. Processing of XML messages is trivial, since there are many ready-to-use libraries in both Java and C++. ICE also allows seamless integration various operating systems (e.g., Windows XP and Linux), which are installed on the various subsystem control computers. Subsystems access and control hardware directly or through off-the-shelf Ethernet-based controllers. For example, Galil multi-axis controllers are used with the servo motors for dome rotation and dome shutter operation. Another, example are the TempTrax Model E interfaces for the temperature probes throughout the dome, which communicate via a built-in web server.

While ThCS monitors temperatures within TCS, ThCS also closely interacts with the Telescope Pointing and Tracking System (TPTS),¹⁷ which handles the movement of the telescope and dome. TPTS also provides a wrapper for the telescope mount software provided by the telescope manufacturer DFM Engineering, Inc. One of the TPTS challenges is the alignment of the relatively small dome opening with the optical axis of the telescope. An algorithm is used to find the position required for the dome so that the aperture is in the correct place aligned with the telescope beam, allowing for the offsets between the pivot point of the telescope mount, the center of the telescope light path, and the center of the sphere of the dome. The dome shutter and azimuth drives are then moved so the dome aperture follows the position of the light path during the day. TPTS also controls the dome louvers.

The primary ThCS objective is to provide a stable environment for NST's main optical components, which are located inside an open telescope support structure. Therefore, the temperature of the optical support structure and primary and secondary mirrors has to be closely monitored. The surface of the primary mirror can be actively cooled by regulating the air flow and temperature to a fan driven heat exchanger. The exchanger will provide a

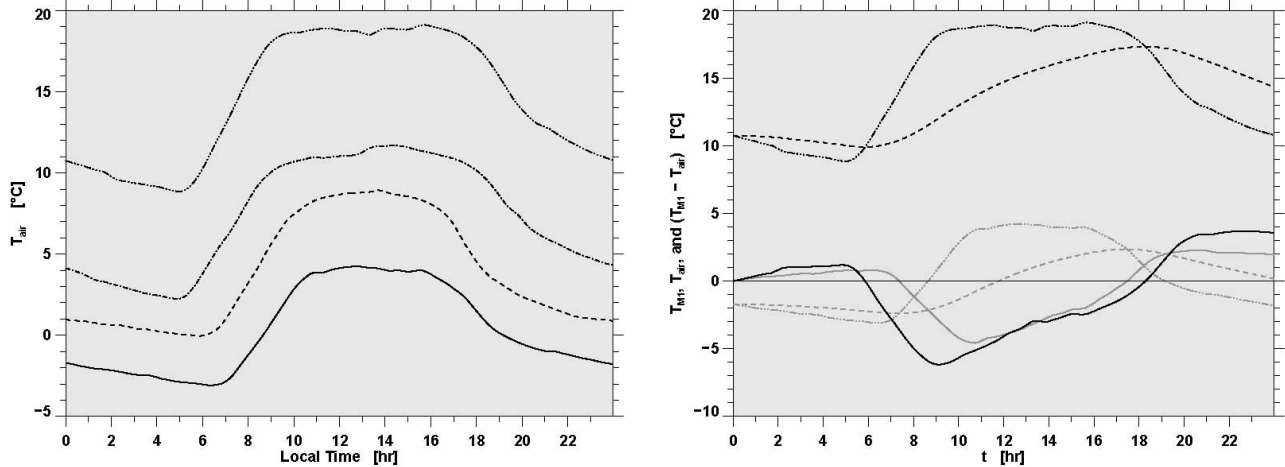


Figure 10. *Left.* Average daily temperature profiles for winter (solid), spring (dashed-dotted), summer (dashed-triple-dotted), and autumn (dashed). *Right.* M1 response (dashed) to ambient air temperature variation (dashed-triple-dotted) during the summer (black) and winter (gray) considering convective heat exchange only. Initially (at midnight), M1 and ambient air temperature are the same. Their temperature differences are given by the solid curves.

laminar flow across the mirror surface, thus avoiding the rise of turbulent eddies from the sunlit mirror surface. The only way to keep the temperature of the telescope structure and other optical components close to ambient is to effectively ventilate the dome and limit the amount of sunlight entering through the dome aperture by making it as small as possible. The radius of the dome aperture is only 20 cm larger than that of the primary mirror. To accomplish the first task, ThCS automatically sends commands to operate the fourteen dome louvers through TPTS to adjust to variable wind speeds and directions during the observing day. Real-time information from a weather station and from a network of temperature probes inside the dome are used in a decision module,^{7,8} which sends the appropriate adjustments through HQ to the dome louvers.

5. THERMAL CONTROL OF THE PRIMARY MIRROR

The thermal control of the primary mirror relies on two different mechanisms: the air inside the dome has to track the outside temperature and a fan driven heat exchanger directs a laminar flow of air across the Sun-facing primary mirror surface. Assuming that the passive ventilation through the the louvers minimizes interior temperature gradients and reduces internal dome seeing, we can use sample temperature profiles for winter, spring, and summer to evaluate the thermal properties of the primary mirror under realistic observing conditions.

Sample profiles for the four seasons are shown in the left panel of Figure 10. These samples were created by averaging all available temperature profiles for the respective seasons. The general shape of all profiles is roughly the same. A fast monotonic temperature rise after sunrise, which reaches a plateau about two hours before local noon. At this time, laminar wind flow across the lake and the lake acting as a heat reservoir balance solar heating and an equilibrium is reached. This plateau persists for up to 10 hours in the summer but lasts only about six hours in the winter. This region of little or no change is not an artifact of the averaging procedure but can also be found in individual daily temperature profiles. Exceptions are days with extended cloud cover. However, since BBSO has more than 300 sunny days per year, cloudy or rainy days only leave an negligible imprint on the averaged seasonal profiles. In the late afternoon and early evening radiative cooling begins, once the Sun sets behind the mountains to the West of the observatory, reaching the coolest temperatures just before sunrise. Typical temperature spreads between day and night are 7.3 K, 9.4 K, 10.3 K, and 9.0 K for winter, spring, summer, and autumn, respectively.

In the right panel of Figure 10, we have chosen two temperature profiles (dashed-triple-dotted curves) for winter (gray) and summer (black) to illustrate how the Zerodur primary responds to changes of the ambient

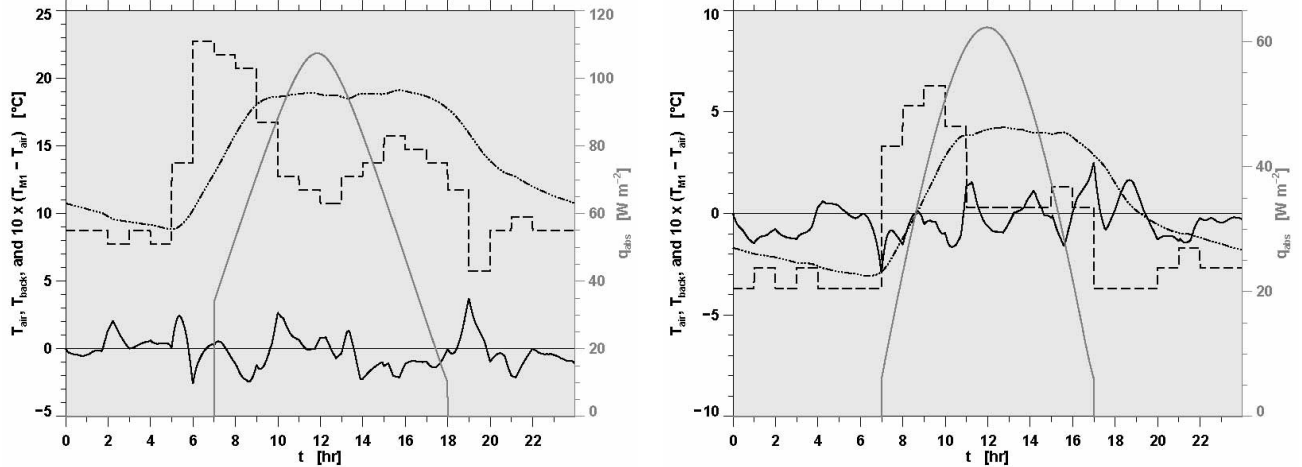


Figure 11. *Left.* Lump capacity model of the primary mirror M1 with realistic temperature profile T_{air} (dashed-triple-dotted) and absorbed solar radiation q_{abs} (solid gray) during the summer months. The air temperature T_{back} (dashed) to convectively cool the backside of M1 is changed every hour in multiples of 1°C to minimize the temperature difference $T_{\text{air}} - T_{\text{M1}}$ (solid black). The temperature difference has been stretched by a factor of 10 to enhance the visibility of small-scale temperature variations. *Right.* Data for winter months (same labeling as in left panel).

temperature (dashed curve). Even without direct exposure to sunlight, the thermal inertia of primary mirror leads to a rapid departure from the ambient temperature. Once the temperature difference exceeds about ± 1 K, mirror seeing becomes an issue and severely limits the performance of a (solar) telescope.

In this introductory example, we assumed that M1 and the surrounding air had the same temperature at midnight. M1 then slowly follows the cooling trend of the ambient air until about sunrise. In fact, it remains within the allowed 1 K temperature envelope for about 1/2 to 1 hour (summer/winter). This agrees with experience gained at older (non-evacuated) solar telescopes, where observations with diffraction-limited quality have been reported for short time periods just after exposing the primary to sunlight. Of course, once these telescopes and their optics heated up, the image quality rapidly deteriorated. The temperature difference between the primary mirror and ambient air $T_{\text{M1}} - T_{\text{air}}$ exceeds the desired 1 K envelope for most of the observing day. In the morning, M1 is cooler by up to 6 K in the summer and 4 K in the winter, respectively. In the late afternoon, the temperature difference reverses sign and reaches values of 4 K in the summer and 2 K in the winter, respectively. As expected, these effects are smaller in the winter than in the summer. The lag of the time-delayed M1 response is about 4 to 6 hours and fine-structures of the air temperature profile are smoothed out. Importantly, M1 now carries excess heat into the next observing day, which would make maintaining the temperature difference in the range of ± 1 K even more difficult. In the following, we will discuss a more realistic scenario adding solar heating and active cooling of the primary mirror to our model.

Starting with the average temperature profiles for summer and winter (see Figure 11), we now add realistic values for the absorbed solar radiation q_{abs} to the lump capacity model. We assume that the observing day starts at 7:00 am local time in the morning and ends at 6:00 pm in the summer and 5:00 pm in the winter (daylight savings time was not taken into account). Furthermore, the observing days were completely sunny with no cloud cover. In principle, both radiation and convection could be used as cooling/heating mechanisms for the primary mirror M1. Since both mechanisms follow the same formal implementation in the M1 lump capacity model, we only discuss convective air cooling/heating of M1. In addition, radiative cooling/heating would require a heat exchanger in close proximity to M1, which is not possible in the tight confines of the M1 support, which houses the actuators for the M1 active optics (aO).

Changing the air temperature T_{back} only every hour in multiples of 1°C , we are able to keep the primary mirror within a few tenth of degree Celsius of the ambient air temperature T_{air} . The rapid rise of the ambient air temperature in the morning requires warming M1 by blowing heated air on the backside. Solar loading

by itself is not sufficient to bring M1 fast enough to the desired temperature. The early morning presents therefore the greatest challenge for controlling the M1 thermal environment. Since the backside air temperature T_{back} is almost 15 °C warmer than the ambient air temperature T_{air} , it is essential the backside of the primary mirror cell is tightly sealed to avoid an exchange of air. A similar but inverted control challenge exists in the late afternoon, when M1 has to be cooled to follow the ambient air temperature. However, the temperature differentials are not as severe. As expected, the control requirements are much more relaxed in the winter time, since the day/night temperature difference are much smaller and so is the solar loading. If a predictive model of the daytime temperature exists, the thermal control of the primary mirror becomes feasible. This is certainly the case for sunny days. However, on partially cloudy days daytime temperature predictions become a challenge and it might not be possible to keep M1 within the ± 1 °C operating envelope. On the other hand, the large clear time fraction at BBSO with more than 300 sunny days, allows to keep the primary mirror within the temperature margins for most of the time.

One concern of the non-isotropic M1 heating/cooling is that the primary mirror can become distorted as a result of thermal gradients. This distortion is proportional to the coefficient of thermal expansion (CTE) of the mirror material. The CTE of Zerodur is $\alpha = 0.00 \pm 0.10 \times 10^{-6} \text{ K}^{-1}$ from 0° – 50° C. The major effect is a dominant axial thermal gradient resulting primarily in a focus error, which can be compensated by changing the distance between the primary mirror and the secondary mirror assembly, which is mounted on a hexapod. However, the actual thermal deformation of the primary mirror will be more complex. This deformation has to be monitored by a dedicated wavefront sensor, which also measures the slowly varying gravitational mirror deformations. These data are fed to a control loop of the mirror support system.¹⁸ The aO support of the primary mirror consists of 36 actuators in three concentric circles (6, 12, and 18 actuators at $r_i = 21.8$ cm, 49.1 cm, and 75.1 cm, respectively). Any residual gravitational or thermal deformations of the primary mirror, which cannot be aO-corrected, have to be compensated by NST’s AO system, which is based on the existing BBSO AO system for the now obsolete 65 cm vacuum reflector.¹⁹

6. CONCLUSIONS

Controlling the thermal environment of the next generation of solar telescopes will be a major challenge considering the necessarily “open-design” of solar telescopes breaking the 1-meter aperture barrier. We have presented results of some initial studies to characterize the BBSO site characteristics and the dome environment in which the future NST will operate. The time-delayed response of NST’s 10-cm thick Zerodur primary mirror to changes of the ambient temperature requires a detailed understanding of its thermal environment and active measures to keep the mirror as close to the ambient temperature as possible. For example, daily temperature predictions become important to determine the optimal temperature of the primary mirror in the morning. An adaptive scheme to operate the dome louvers has to be developed, which equalizes the air temperature inside and outside of the dome, while avoiding wind-shake problems of the optical support structure, especially for the exposed outrigger that carries the secondary mirror assembly. Our work has shown that NST can achieve its expected performance, even in the challenging daytime thermal environment. However, the results of our studies have to be confirmed and refined in the engineering first-light phase, which is expected to begin in late 2007. Commissioning of NST (first-light) is expected about 12 months later.

7. ACKNOWLEDGMENTS

This work was supported by NSF under grants ATM 00-342560, ATM 02-36945, IIS ITR 03-24816 and AST MRI 00-79482 and by NASA under grant NNG0-6GC81G. We would like to thank Nathan Dalrymple for providing the initial programs to perform the thermal modeling of the primary mirror and Tom Spirock for providing some of the BBSO pictures.

REFERENCES

1. F. Hill, J. Beckers, P. Brandt, J. Briggs, T. Brown, W. Brown, M. Collados, C. Denker, S. Fletcher, S. Hegwer, T. Horst, M. Komsa, J. Kuhn, A. Lecinski, H. Lin, S. Oncley, M. Penn, T. R. Rimmele, H. Socas-Navarro, and K. Streander, “Solar Site Testing for the Advanced Technology Solar Telescope,” in *Ground-Based Telescopes*, J. M. Oschmann, ed., *Proceedings of SPIE* **5489**, pp. 122–129, 2004.

2. H. Socas-Navarro, J. Beckers, P. Brandt, J. Briggs, T. Brown, W. Brown, M. Collados, C. Denker, S. Fletcher, S. Hegwer, F. Hill, T. Horst, M. Komsa, J. Kuhn, A. Lecinski, H. Lin, S. Oncley, M. Penn, T. Rimmele, and K. Streander, "Solar Site Survey for the Advanced Technology Solar Telescope. I. Analysis of the Seeing Data," *Publ. Astron. Soc. Pac.* **117**, pp. 1296–1305, 2005.
3. A. P. Verdoni and C. Denker, "The Local Seeing Environment at Big Bear Solar Observatory," *Publ. Astron. Soc. Pac.* **119**, pp. 793–804, 2007.
4. P. T. Gallagher, C. Denker, V. Yurchyshyn, T. Spirock, J. Qiu, H. Wang, and P. R. Goode, "Solar Activity Monitoring and Forecasting Capabilities at Big Bear Solar Observatory," *Ann. Geophys.* **20**, pp. 1105–1115, 2002.
5. P. R. Goode, C. Denker, L. I. Didkovsky, J. R. Kuhn, and H. Wang, "1.6-Meter Solar Telescope in Big Bear – The NST," *J. Korean Astron. Soc.* **36**, pp. 125–133, 2003.
6. C. Denker, P. R. Goode, D. Ren, M. A. Saadeghvaziri, A. P. Verdoni, H. Wang, G. Yang, V. Abramenko, W. Cao, R. Coulter, R. Fear, J. Nenow, S. Shoumko, T. J. Spirock, J. R. Varsik, J. Chae, J. R. Kuhn, Y. Moon, Y. D. Park, and A. Tritschler, "Progress on the 1.6-Meter New Solar Telescope at Big Bear Solar Observatory," in *Ground-Based and Airborne Telescopes*, L. M. Stepp, ed., *Proceedings of SPIE* **6267**, p. 62670A, 2006.
7. C. Denker and A. P. Verdoni, "Integrating Seeing Measurements into the Operations of Solar Telescopes," in *Ground-Based and Airborne Telescopes*, L. M. Stepp, ed., *Proceedings of SPIE* **6267**, p. 62670L, 2006.
8. A. P. Verdoni and C. Denker, "The Thermal Control Systems of the New Solar Telescope at Big Bear Solar Observatory," in *Ground-Based and Airborne Telescopes*, L. M. Stepp, ed., *Proceedings of SPIE* **6267**, p. 62670M, 2006.
9. J. U. Teran, D. S. Porter, E. A. Hileman, and D. H. Neff, "Unique Dome Design for the SOAR Telescope Project," in *Telescope Structures, Enclosures, Controls, Assembly/Integration/Validation, and Commissioning*, T. A. Sebring and T. Andersen, eds., *Proceedings of SPIE* **4004**, pp. 155–163, 2000.
10. H. M. Martin, J. H. Burge, B. Cuerden, S. M. Miller, B. Smith, and C. Zhao, "Manufacture of 8.4-m Off-Axis Segments: A 1/5-Scale Demonstration," in *Optical Fabrication, Metrology, and Material Advancements for Telescopes*, E. Atad-Ettinger and P. Dierickx, eds., *Proceedings of SPIE* **5494**, pp. 62–70, 2004.
11. H. Hu and W. Timothy Liu, "Oceanic Thermal and Biological Responses to Santa Ana Winds," *Geophys. Res. Lett.* **30**, pp. 50–1, 2003.
12. P. Montañés-Rodríguez, E. Pallé, P. R. Goode, J. Hickey, and S. E. Koonin, "Globally Integrated Measurements of the Earth's Visible Spectral Albedo," *Astrophys. J.* **629**, pp. 1175–1182, 2005.
13. J. D. Giorgini, D. K. Yeomans, A. B. Chamberlin, P. W. Chodas, R. A. Jacobson, M. S. Keesey, J. H. Lieske, S. J. Ostro, E. M. Standish, and R. N. Wimberly, "JPL's On-Line Solar System Data Service," *Bull. Am. Astron. Soc.* **28**, p. 1158, 1996.
14. F. Hill, G. Fischer, S. Forgach, J. Grier, J. W. Leibacher, H. P. Jones, P. B. Jones, R. Kupke, R. T. Stebbins, and D. W. Clay, "The Global Oscillation Network Group Site Survey. 2. Results," *Sol. Phys.* **152**, pp. 351–379, 1994.
15. G. Yang, J. R. Varsik, S. Shumko, C. Denker, S. Choi, and H. Wang, "The Telescope Control System of the New Solar Telescope at Big Bear Solar Observatory," in *Advanced Software and Control for Astronomy*, H. Lewis and A. Bridger, eds., *Proceedings of SPIE* **6274**, p. 62741Y, 2006.
16. S. Shumko and G. Yang, "Object-Oriented Communications for the NST's Telescope Control System: Design and Implementation," in *Advanced Software and Control for Astronomy*, H. Lewis and A. Bridger, eds., *Proceedings of SPIE* **6274**, p. 62741Q, 2006.
17. J. R. Varsik and G. Yang, "Design of a Telescope Pointing and Tracking Subsystem for the Big Bear Solar Observatory New Solar Telescope," in *Advanced Software and Control for Astronomy*, H. Lewis and A. Bridger, eds., *Proceedings of SPIE* **6274**, p. 62741T, 2006.
18. G. Yang, "Design and Implementation of the Primary and Secondary Mirror Control System for NST," in *Advanced Software and Control for Astronomy*, H. Lewis and A. Bridger, eds., *Proceedings of SPIE* **6274**, p. 62740Z, 2006.
19. C. Denker, A. Tritschler, T. R. Rimmele, K. Richards, S. L. Hegwer, and F. Wöger, "Adaptive Optics at the Big Bear Solar Observatory: Instrument Description and First Observations," *Publ. Astron. Soc. Pac.* **119**, pp. 170–182, 2007.